Interferogram formation in the presence of complex and large deformation

Sang-Ho Yun,[1] Howard Zebker,[1] Paul Segall,[1] Andrew Hooper,[2] and Michael Poland[3]

[1] Sierra Negra volcano in Isabela island, Galápagos, erupted from October 22 to October 30 in 2005. During the 8 days of eruption, the center of Sierra Negra's caldera subsided about 5.4 meters. Three hours prior to the onset of the eruption, an earthquake (Mw 5.4) occurred, near the caldera. Because of the large and complex phase gradient due to the huge subsidence and the earthquake, it is difficult to form an interferogram inside the caldera that spans the eruption. The deformation is so large and spatially variable that the approximations used in existing InSAR software (ROI, ROI_PAC, DORIS, GAMMA) cannot properly coregister SAR image pairs spanning the eruption. We have developed here a two-step algorithm that can form intra-caldera interferograms from these data. The first step involves a "rubber-sheeting" SAR image coregistration. In the second step we use range offset estimates to mitigate the steep phase gradient. Using this new algorithm, we retrieve an interferogram with the best coverage to date inside the caldera of Sierra Negra. **Citation:** Yun, S.-H., H. Zebker, P. Segall, A. Hooper, and M. Poland (2007), Interferogram formation in the presence of complex and large deformation, *Geophys. Res. Lett.*, *34*, L12305, doi:10.1029/2007GL029745.

1. Introduction

[2] The phase difference between two SAR images is directly proportional to range change, and it depends on imaging geometry, topography, deformation, and atmospheric delay. A critical step in InSAR processing is SAR image coregistration. In order to form a high-quality interferogram, SAR image coregistration must be accurate to within a fraction of a pixel. This is usually implemented by cross-correlating small blocks of one SAR image (here denoted the "slave" image) with the other SAR image ("master" image). Repeated at many locations distributed throughout the entire image, the set of cross-correlations produces separate grids of the range and azimuth components of the offset fields. Interpolating the sparse estimate of the offset fields using a polynomial surface model yields the registration parameters at all locations.

$$p(x,y) = \sum_{i+j \leq n} c_{ij} x^i y^j \qquad (1)$$

[3] Here x and y are the locations of each pixel, i and j are all possible non-negative integer pair whose sum is not greater than n, and c_{ij} is a constant for each x^i and y^j combination. For example, ROI_PAC [*Rosen et al.*, 2004] uses a quadratic polynomial (i.e. $n = 2$), while DORIS [*Kampes and Usai*, 1999] and GAMMA [*Werner et al.*, 2000] can accommodate up to a fourth-order polynomial. Once the best-fit polynomial surface is determined, the slave image is coregistered by resampling at the master image coordinates. However, for the Sierra Negra data the fourth-order polynomial is not sufficiently spatially variable, and thus the offset fields of SAR images that span the eruption cannot be fit by a simple polynomial. We have not tested DIAPASON [*Massonnet*, 1997], another standard InSAR software.

[4] This effect is due to large and complex deformation. The eruption was preceded by an earthquake somewhere near the caldera. The magnitude of the earthquake is Mw 5.4, large enough to produce at least 1 m of range change, as measured from the range offsets [*Jónsson et al.*, 2005]. Moreover, the eruption occurred through a fissure along the northern rim of caldera. Thus, there was also deformation associated with the dike intrusion. The total deformation is the sum of these events plus subsidence during the eruption. We measure about 4.3 meters of maximum range increase, equivalent to about 5.4 meters of subsidence. Given that the strong deformation is confined within the caldera, whose dimension is 4.4 km in radius, the average strain caused by these events is about 1.2×10^{-3}. The theoretical limit of maximum detectable strain is half the wavelength divided by the pixel spacing [*Massonnet and Feigl*, 1998], and for a nominal C-band strip mode (wavelength = 5.6 cm, pixel spacing = 20 m) this is about 1.4×10^{-3}. As the coherence becomes smaller the maximum detectable strain decreases. *Baran et al.* [2005] deduced a functional model of this relationship from both real and synthetic data. For a coherence of about 0.3, which is the case of this study, their functional model predicts that the maximum detectable strain becomes zero. This implies that forming an intra-caldera interferogram of 2005 eruption at Sierra Negra is a real challenge.

[5] Using the existing standard InSAR software packages, we were not able to form an interferogram inside the caldera. Without exception, all the interferograms that span the eruption failed to show fringes inside the caldera, when analyzed with polynomial registration algorithms. A typical interferogram before unwrapping is shown in Figure 1, produced using the GAMMA software. Hence we have developed a new approach to achieve InSAR coregistration that is more robust than the conventional methods for large and complex deformation. This new algorithm consists of two distinct steps: 1) co-registering the master and slave

[1]Department of Geophysics, Stanford University, Stanford, California, USA.
[2]Nordic Volcanological Center, University of Iceland, Reykjavik, Iceland.
[3]Hawaiian Volcano Observatory, U.S. Geological Survey, Hawaii National Park, Hawaii, USA.
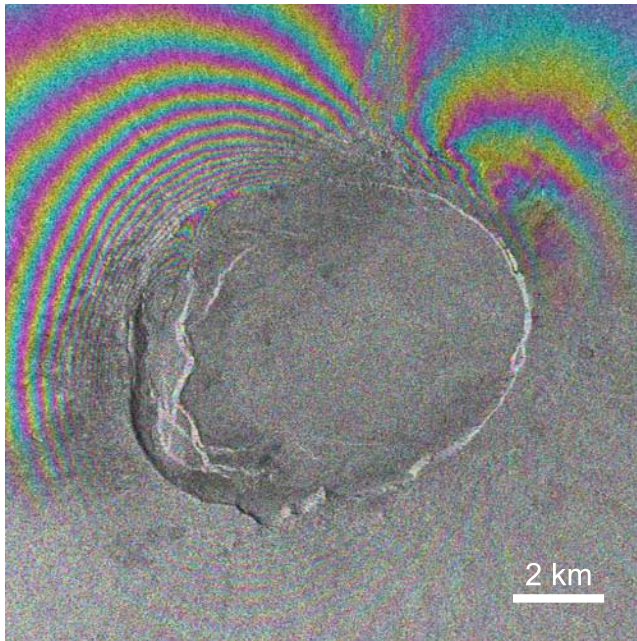
Figure 1. Co-eruptive interferogram processed by GAMMA software using Envisat data (beam IS 5, track 376, 2005/10/16 – 2005/11/20).

images using a "rubber-sheet" approach, and 2) reducing the displacement gradient using information from amplitude range offsets. The first step is to coregister a slave single-look complex (SLC) image to a master SLC, and the second step is for mitigating the steep phase gradient due to the large deformation.

2. Range and Azimuth Offset

[6] Consider a slave image printed on a rubber sheet, and overlay it with a master image. Then distort the slave image differently in different locations to match the features in the master image. This is the concept of rubber sheeting, a colloquial term used in image processing. In our application, we use range and azimuth offsets to get the local distortion information.

[7] We use square subimage blocks to cross-correlate two single-look SAR amplitude images. The size of the blocks affects the accuracy and the resolution of the cross-correlation results. Increasing the block size increases the accuracy while reducing the resolution. We find that 32-by-32 pixel blocks produce a good result. For 16-by-16 block size the range offset uncertainty becomes about 1 m inside the caldera, making the accuracy marginally acceptable. A block size of 64-by-64 causes lower resolution and increases the size of the artifact of the cross-correlation, described later in this section. For this study we form the densest possible offset vector field by implementing the cross-correlation at every single pixel in the image, as we want to see the effect of smoothing. For practical purpose one can produce a sparser offset field by evaluating every 8 pixels or every 16 pixels.

[8] Figure 2 shows a single look range and azimuth offset image in the radar coordinate system. We work with

single look images in radar coordinates through the phase unwrapping step, in order to minimize the risk of spatial aliasing due to the large deformation. The range and azimuth offset images are noisy, showing a characteristic cross-hair artifact pattern (Figure 2). Bright scatterers tend to dominate the offset field inside every block in which they are included. In Figures 2e and 2f, the size of the cross-hair patterns is about the size of the cross-correlation block. We apply a Gaussian smoothing filter to suppress the high-frequency noise, which we describe later in this paper.

3. Unbiased Masking of Noise

[9] Before smoothing the offset images, we mask out noise-dominant areas, where offset values are unrealistically small or large. Determining the boundary of the mask is not a trivial task, because coherence information is not readily available due to the large and complex deformation. We find that the cumulative distribution function (cdf) of offset values provide a clear guide for masking. Figure 3 shows the cumulative histograms of (a) range and (b) azimuth offset inside the caldera. The slope of the cdf in the noisy areas is much smaller than that for valid areas. We use piecewise linear fitting (red lines) to the cdf; the thresholds for masking are given by the intersections of the fitting lines.

4. Smoothing for Resampling

[10] Once the noisy areas are masked, we smooth the offset fields by filtering. We have tested a moving average filter, a median filter, and a Gaussian smoothing filter. We find that a Gaussian smoothing filter produced interferograms with the highest correlation. Our Gaussian smoothing filter is circular with width σ. The radius of the filter is set 2.634σ, so the weight of the kernel at its edge is 1/32, the nominal theoretical accuracy of cross-correlation with 32×32 pixel block.

[11] We find that the coregistration based on rubber-sheeting interpolation is robust for a wide range of Gaussian widths σ. As σ varies from 0 to 10 pixels, the mean coherence increases rapidly from 0.329 to 0.454 for caldera and from 0.555 to 0.809 for north flank. After hitting the maxima ($\sigma = 10$ pixels for caldera and $\sigma = 7$ pixels for north flank), the mean coherence does not vary significantly until $\sigma = 50$ pixels, where we stopped the experiment. Note that the Gaussian smoothing kernel with $\sigma = 10$ pixels and a radius of 26.34 pixels is an efficient filter size that reduces the cross-hair artifacts of 32×32 pixels. Using a circular median filter, the maximum mean coherence occurs when the radius is 16 pixels, which is again of comparable size to a 32×32 block.

5. Resampling

[12] Most SAR data are near-critically sampled in both the range and azimuth directions. In other words, the sampling frequencies are slightly greater than the two-sided signal bandwidth in both directions. Thus, sinc-type interpolation is preferred for SAR image registration. We use a raised cosine (RC) interpolation kernel suggested by *Cho et al.* [2005], which is a sinc-type interpolation but has smaller
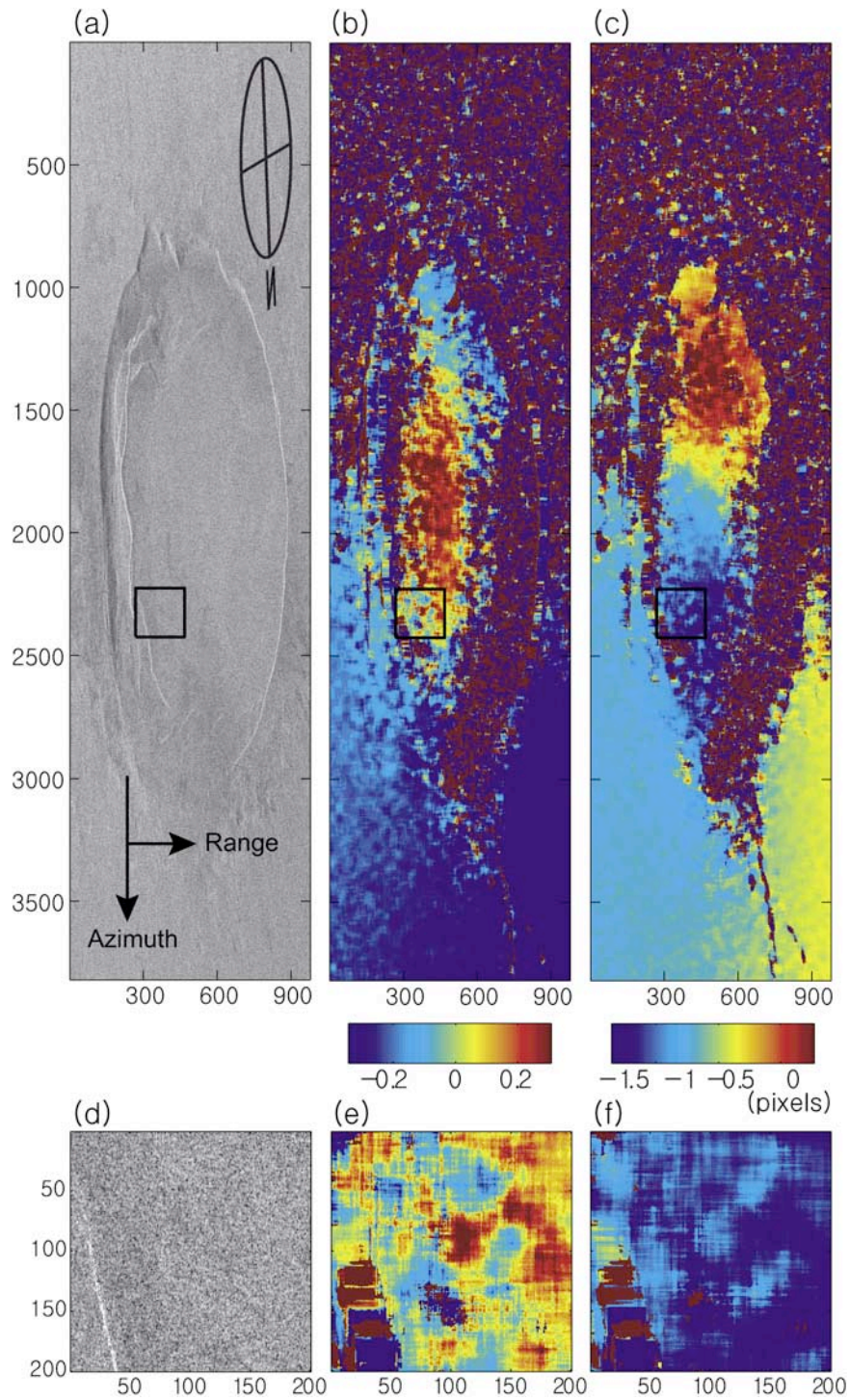
Figure 2. Single look (a) amplitude, (b) range offset, (c) azimuth offset in radar coordinate system with pixel spacings of 7.8 m in slant range and 3.2 m in azimuth direction. The upside-down and elongated circular map compass show how features look different compared to georeferenced frame. (d–f)The enlargement of the black box in Figures 2a–2c.

phase error due to resampling than the plain sinc interpolation. Combining a sinc with a raised cosine function as used in digital communications, one can write the 2-D version impulse response $i(x, y)$ as

$$i(x, y) = \text{sinc}(x, y) \frac{\cos(\alpha \pi x) \cos(\beta \pi y)}{(1 - 4\alpha^2 x^2)(1 - 4\beta^2 y^2)} \text{rect}\left(\frac{x}{L}, \frac{y}{L}\right) \quad (2)$$

where $\text{sinc}(x, y)$ means $\text{sinc}(x)\text{sinc}(y)$, and L is the kernel size, and α and β are roll-off factors with values between 0 and 1, and $\text{rect}(\frac{x}{L}, \frac{y}{L})$ is a 2-D unit boxcar function whose value is one inside a square of size L and zero elsewhere. When $\alpha = 0$ and $\beta = 0$, Equation (2) becomes a 2-D sinc interpolator. As α and β grow larger, the interferometric phase error becomes larger, but the sidelobes of $i(x, y)$ are suppressed, relaxing the effect of the finite kernel size. The
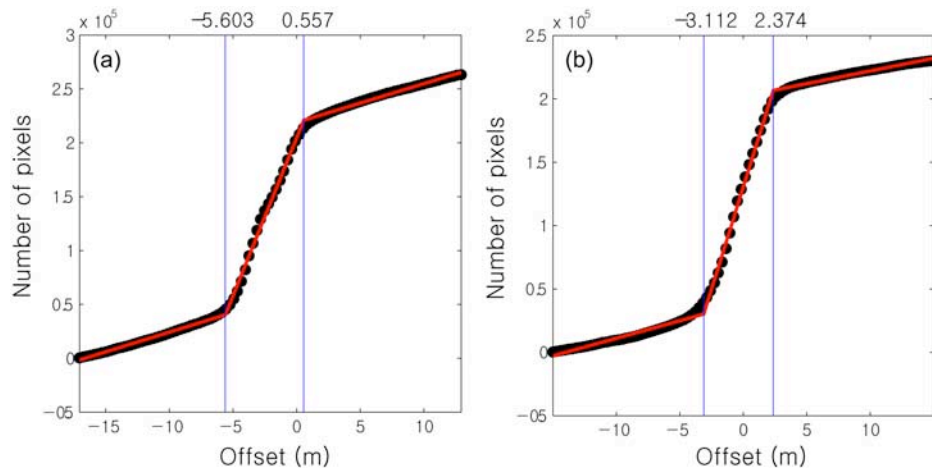
Figure 3. Cumulative histogram of (a) range and (b) azimuth offset values inside the caldera.
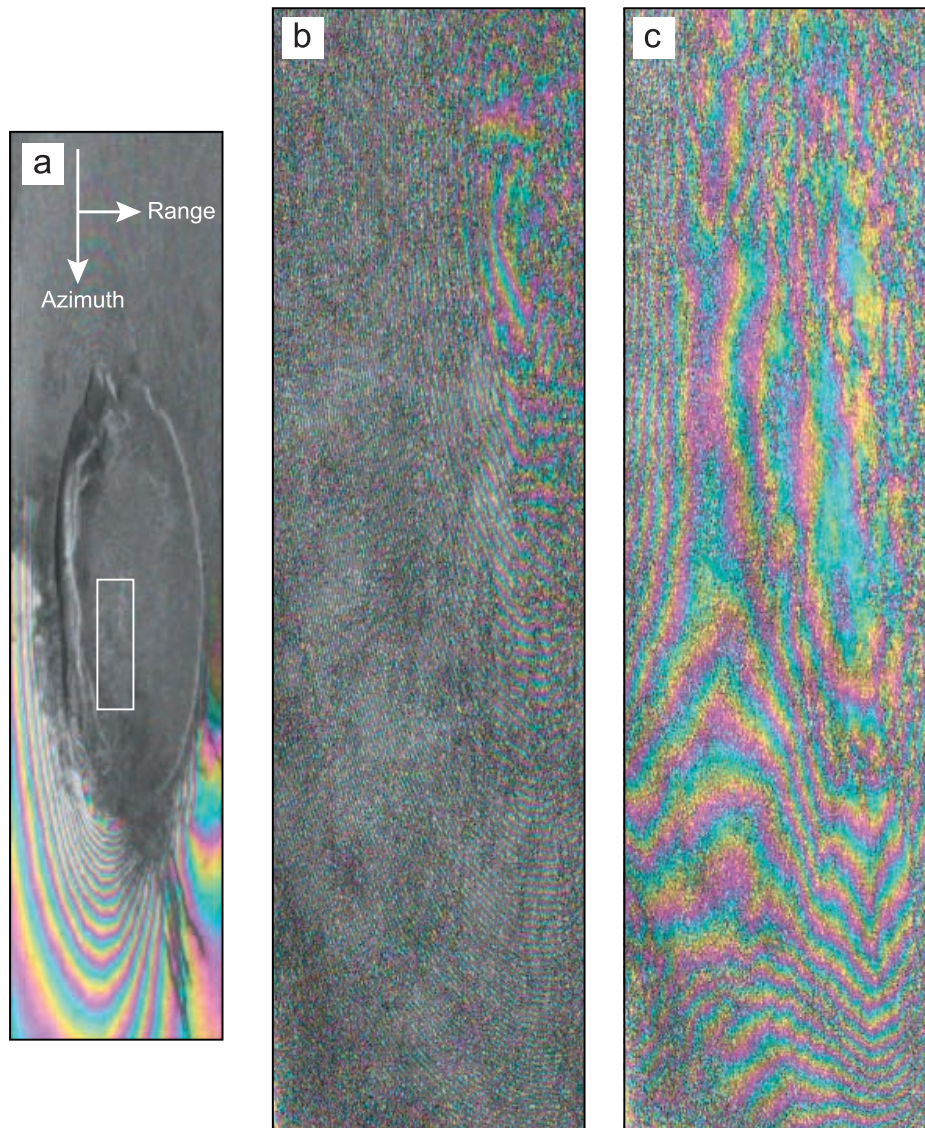

Figure 4. (a) Deformation interferogram after the rubber-sheeting SAR coregistration. (b) Enlargement of the white box in Figure 4a. (c) Subtracting the range offset decreases the displacement gradient, allowing unwrapping the phase over a larger area.
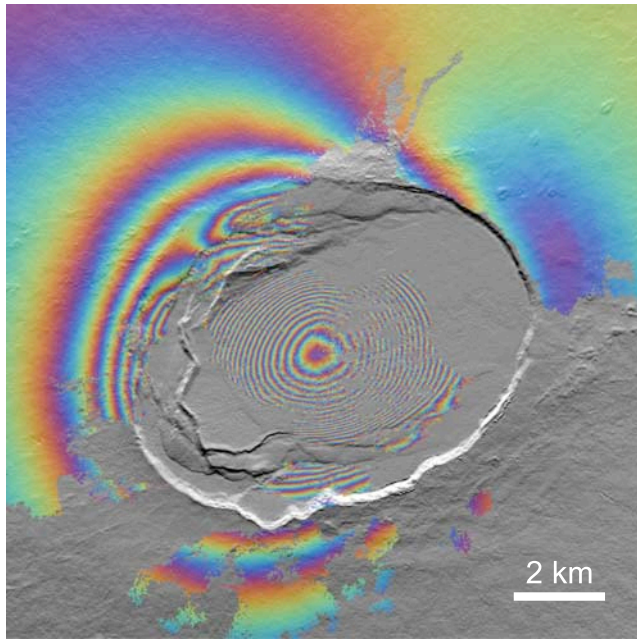
Figure 5. Final interferogram from the same SAR images used to produce Figure 1. One color fringe represents 15 cm of range change.

optimum values of α and β that satisfy the Nyquist criterion are [*Cho et al.*, 2005]

$$\alpha = 1 - \frac{B_r}{f_{sr}} = 1 - \frac{1}{\chi_r} \qquad (3)$$

$$\beta = 1 - \frac{B_a}{f_{sa}} = 1 - \frac{1}{\chi_a} \qquad (4)$$

where χ_r and χ_a are oversampling factors (i.e. sampling frequency divided by bandwidth) in range and azimuth respectively. In this study $\chi_r = 1.2005$ and $\chi_a = 1.1588$ were used. Prior to the resampling, we estimate and subtract the carrier phase both in range and azimuth direction. This is to ensure that dominant energy is not lost during resampling, which is a low-pass filter. After resampling, we add the estimated carrier phase back to the data.

6. Range Offset as a Proxy for Interferogram Phase

[13] All phase unwrapping algorithms are based on the assumption that the input interferogram phase is not aliased in most places. This assumption does not hold in regions of large deformation. Aliasing can be reduced by subtracting an estimate of the interferogram phase before unwrapping. When there is no independent information on the rough shape of the deformation, the range offset image can be used to construct the estimated interferogram.

[14] A range offset field contains the same information as an interferogram [*Amelung et al.*, 2000; *Jónsson et al.*, 2005], except that it has a different noise character and magnitude. *Bamler* [2000] derived the standard deviation of

an offset estimated from cross-correlation of amplitude images for homogeneous (i.e. featureless) image patches to

$$\sigma_{\text{ampoffset}} = \sqrt{\frac{3}{2N}} \frac{\sqrt{1-\rho^2}}{\pi\rho} \chi^{3/2} \qquad (5)$$

where ρ is the interferometric coherence, and N is the number of samples in the cross-correlation block, and χ is the oversampling factor. Using a coherence of 0.4, an oversampling factor of 1.2, and a pixel spacing of 7.8 m in range, we calculate the range offset uncertainty of about 30 cm. Note that this is the lower bound, since topography will add noise (Figure 2e and 2f). Nevertheless, this calculation shows that the signal-to-noise ratio of the range offset is large enough that we can use the range offset as a proxy for interferometric phase, after suppressing the noise with smoothing.

[15] We smooth the range offset image with a Gaussian smoothing kernel of $\sigma = 50$ pixels and a kernel radius of 132 pixels. The smoothed range offset is subtracted from the interferogram before phase unwrapping and later added back, after unwrapping. When smoothing the range offset, one should keep two things in mind. First, all the natural features including deformation in a single-look interferogram are elongated in the azimuth direction. Thus, the shape of the interpolation kernel should also be elongated by the same factor. Alternatively, one can take average in azimuth to make the pixels square and apply an equidimensional smoothing kernel, and then stretch the result back to the single-look coordinate. Usually, the latter approach is more efficient.

[16] Second, deformation signals in interferograms are projections of 3-D surface displacement vector field onto a slant line of sight between the radar and the target. Thus, a circularly symmetric surface deformation causes asymmetric interferometric phase. Applying a large symmetric smoothing filter can distort the pattern of asymmetry. Distortion can also be caused by errors in the range offset that were not properly masked out in the first step. In this study we are able to identify a small faint concentric peak signal at the center of caldera in the interferogram before subtracting the range offset. Then we simply shift (about 40 pixels toward an increasing range direction) the location of the smoothed range offset to match the observed peak with that of the range offset.

[17] Figure 4 shows the effect of range offset subtraction. The single-look interferogram of deformation (Figure 4a) is the result of rubber-sheeting coregistration. Despite the improved coherence, the fringes are still not visible due to the large phase gradient. In the enlargement of the white box (Figure 4b) the maximum subsidence is shown in the upper right corner. The displacement gradient is high close to the critical value in the azimuth direction. This problem is more severe in range direction and the fringes become aliased toward the left. When the range offset is subtracted (Figure 4c) the displacement gradient becomes much smaller.

[18] SNAPHU [*Chen and Zebker*, 2001] was used for phase unwrapping. Figure 5 shows the final interferogram with fairly good coverage inside the caldera. The eastern part of the caldera was completely decorrelated due to the lava flow during the eruption, and the western part of the

caldera was decorrelated possibly due to the earthquake occurred 3 hours prior to the onset of the eruption.

7. Conclusion

[19] Using a rubber-sheeting coregistration scheme, we were able to improve the interferometric coherence inside the caldera for InSAR data that span the 2005 eruption at Sierra Negra Volcano, Galápagos. Based on the smoothed range and azimuth offset images, resampling was done with a raised cosine interpolation kernel. We subtracted an even smoother and slightly shifted version of the range offset from the interferogram of the coregistered pair. These steps enable us to form a useful interferogram inside the caldera of the volcano (see Figure 5). The fringe on the south flank is from separate processing using ROI_PAC, applying an adaptive power spectrum filter [*Goldstein and Werner*, 1998] twice to enhance the narrow-band signal (the hint of fringes in Figure 1) against the broad-band noise (vegetation-induced decorrelation). Our two step algorithm depends on the coverage of the range and azimuth offsets.

[20] Auxiliary materials are also available[1]. They provide the detailed performance of the algorithm proposed in this study.

---

[1]Auxiliary materials are available in the HTML. doi:10.1029/2007GL029745.

References

Amelung, F., S. Jónsson, H. Zebker, and P. Segall (2000), Widespread uplift and 'trapdoor' faulting on galapagos volcanoes observed with radar interferometry, *Nature*, *407*(6807), 993–996.

Bamler, R. (2000), Interferometric stereo radargrammetry: Absolute height determination from ers-envisat interferograms, *Eur. Space Agency Spec. Publ., ESA SP 2*, 742–745.

Baran, I., M. Stewart, and S. Claessens (2005), A new functional model for determining minimum and maximum detectable deformation gradient resolved by satellite radar interferometry, *IEEE Trans. Geosci. Remote Sens.*, *43*, 675–682.

Chen, C. W., and H. A. Zebker (2001), Two-dimensional phase unwrapping with use of statistical models for cost functions in nonlinear optimization, *J. Opt. Soc. Am. A Opt. Image Sci.*, *18*(2), 338–351.

Cho, B. L., Y. K. Kong, and Y. S. Kim (2005), Interpolation using optimum Nyquist filter for SAR interferometry, *J. Electromagn. Waves Appl.*, *19*(1), 129–135.

Goldstein, R. M., and C. L. Werner (1998), Radar interferogram filtering for geophysical applications, *Geophys. Res. Lett.*, *25*(21), 4035–4038.

Jónsson, S., H. Zebker, and F. Amelung (2005), On trapdoor faulting at Sierra Negra volcano, Galápagos, *J. Volcanol. Geotherm. Res.*, *144*, 59–71.

Kampes, B., and S. Usai (1999), Doris: The Delft Object-oriented Radar Interferometric Software, paper presented at ITC 2nd ORS Symposium, Int. Inst. for Geoinf. Sci. and Earth Obs., Enschede, Netherlands.

Massonnet, D. (1997), Producing ground deformation maps automatically: The DIAPASON concept, *IEEE Trans. Geosci. Remote Sensing*, *3*, 1338–1340.

Massonnet, D., and K. L. Feigl (1998), Radar interferometry and its application to changes in the Earth's surface, *Rev. Geophys.*, *36*(4), 441–500.

Rosen, P. A., S. Hensley, G. Peltzer, and M. Simons (2004), Updated repeat orbit interferometry package released, *Eos Trans. AGU*, *85*(5), 47.

Werner, C., U. Wegmuller, T. Strozzi, and A. Wiesmann (2000), Gamma SAR and interferometric processing software, paper presented at ERS-ENVISAT Symposium, Eur. Space Agency, Gothenburg, Sweden.

A. Hooper, Nordic Volcanological Center, University of Iceland, Sturlugata 7, 101 Reykjavik, Iceland. (ahooper@hi.is)

M. Poland, Hawaiian Volcano Observatory, U.S. Geological Survey, Reginald Okamura Building, Crater Rim Road, Hawaii National Park, HI 96718, USA. (mpoland@usgs.gov)

P. Segall, S.-H. Yun, and H. Zebker, Department of Geophysics, Stanford University Stanford, CA 94305, USA. (segall@pangea.stanford.edu; shyun@stanford.edu; zebker@stanford.edu)